Rivulet Flow In Vertical Parallel-Wall Channels

G. E. McCreery
P. Meakin
D. M. McEligot

April 2005

INL
Idaho National
Laboratory

Rivulet flow in vertical parallel-wall channels

Project: Multiphase flow in complex fracture apertures under a wide range of flow conditions
DoE EM Science program
Technical report

G. E. McCreery, P. Meakin and D. M. McEligot

_10_ April 2006

Rivulet flow in vertical parallel-wall channels

G. E. McCreery, P. Meakin and D. M. McEligot

Table of contents

In comparison with studies of rivulet flow over external surfaces, rivulet flow confined by two surfaces has received almost no attention. Fully-developed rivulet flow in vertical parallel-wall channels was characterized, both experimentally and analytically for flows intermediate between a lower flow limit of drop flow and an upper limit where the rivulets meander. Although this regime is the most simple rivulet flow regime, it does not appear to have been previously investigated in detail.   Experiments were performed which measured rivulet widths for aperture spacing ranging from 0.152 mm to 0.914 mm. The results were compared with a simple steady-state analytical model for laminar flow. The model divides the rivulet cross-section into an inner region, which is dominated by viscous and gravitational forces and where essentially all flow is assumed to occur, and an outer region, dominated by capillary forces, where the geometry is determined by the contact angle between the fluid and the wall. Calculations using the model provided excellent agreement with data for inner rivulet widths and good agreement with measurements of outer rivulet widths.

---

1.   Introduction

Rivulet flow with a free upper surface over external solid substrates has been studied extensively during the past four decades. In one of the first studies, Hartley and Murgatroyd (1964) characterized the falling-film-to-rivulet-flow transition using both force and energy criteria. Over time, this work was followed by many other studies that described the film-to-rivulet transition, rivulet geometry, rivulet stability and the transition to meandering flow. A few examples include studies by Towell and Rothfeld (1966), Mikielewicz and Moszynski (1976), Bentwich *et al.* (1976), Young and Davis (1987), Schmuki and Laso (1990), Hughes and Bott (1998), and Johnson *et al*. (1999).   Much of the rivulet flow research has been motivated by the need to characterize heat and mass transfer for high-flux heat exchangers cooled by external flow and by geophysical applications. Predictions of the transition from thin film flow to rivulet flow and the rivulet flow geometry provides the flow boundary conditions and heat transfer area for convection to the flowing liquid. An example is the work by McCreery *et al.* (1989), who studied falling film and rivulet flow distributions and heat transfer for a heated steam generator tube in a vertical orientation.

The work reported in this manuscript was motivated by the need to obtain a better understanding of fluid flow and the transport of contaminants, such as toxic metals and radionuclides, in fractures in the Earth's subsurface. The formation and travel of rivulets allows water and associated contaminants to penetrate further and faster into the subsurface than for film flow. The transition from film flow to rivulet flow is expected to be particularly significant for the penetration of water into partially-saturated fractured porous materials since reduction in the contact area between the invading fluid and the fracture surfaces will reduce loss of fluid from the fracture aperture by imbibition into the porous matrix. Channeling the flow into rivulets will therefore allow the fluid remaining in the fracture to penetrate further and faster.

In comparison with research on external rivulet flow, rivulet flow confined by two surfaces has received almost no attention despite applications such as flow in geological fractures and liquid cooling of finned heat exchanger tubes. Anand and Bejan (1986) performed an

experimental study and analysis of the transition from laminar to turbulent flow for rivulet flow between parallel plates. The transition was marked by an abrupt change to meandering flow, which the authors described as a phenomenon similar to buckling of fluid layers. Su *et al*. (2001), studied solute transport in unsaturated fractures both experimentally and analytically. Their investigations included intermittent rivulet flow, which the authors characterized as "snapping rivulet" and "pulsating blob" modes. Nicholl and Glass (1994) reported research on the gravity-driven wetting front instability in initially dry fractures with experiments that employed a transparent rough-walled simulated fracture. Gravity-driven instabilities occur when a dense fluid overlies a lighter fluid and the combination of capillary and viscous forces is not sufficient to stabilize the displacement front. The resulting liquid fingers penetrate the fracture. The initial finger width for displacement of gas by liquid may be predicted for flow in narrow parallel-wall channels (*a.k.a.* Hele-Shaw cells) using linear stability theory. A rivulet may be formed when a finger that has propagated through the channel continues to be supplied with liquid. The width of the finger is typically considerably wider than that of the ensuing rivulet because capillary force at the advancing finger tip retards its penetration into the aperture. When fluid is injected at one position at the top of an initially dry parallel channel, the initial flow consists of a large slow-moving drop with a trailing rivulet attached, as shown in Figure 1. If the flow rate is sufficiently large, the rivulet is maintained after the drop has drained. If the flow rate is below a critical lower limit, the rivulet breaks and a new drop with a trailing rivulet will form. The new drop and subsequent drops are smaller and faster moving than the initial drop because wetting is then facilitated by a thin layer of fluid deposited on the walls by the initial drop.

The objectives of the research presented herein were to characterize both experimentally and analytically rivulet flow in channels consisting of the aperture between two solid flat parallel walls aligned vertically. Emphasis was on flows between the lower flow drop regime limit and the upper meandering flow limit.   Although this regime is the most simple rivulet flow regime, it does not appear to have been previously investigated in detail.

2. Analytical model

The analytical model subdivides the rivulet cross-section into two regions, an inner region where the vast majority of the flow is assumed to occur and an outer, no-flow region, where the rivulet is broadened by wall wetting.

2.1 Rivulet inner region

It was observed in our experiments that rivulets contract in width below the injection point (due to fluid acceleration by gravity) and then approach an approximately constant width as fully developed flow is established. The width of a rivulet for steady, fully developed, flow is derived. Since acceleration effects are not considered, the equations of motion (the Navier-Stokes equations) simplify to a balance of viscous and gravitational forces. Derivation of the model is based on the following assumptions:

1. Laminar flow.
2. The pressure gradient in the flow direction is negligible because the imposed air pressure and surface tension forces are constant.
3. Flow is orientated in the vertical downward direction (not meandering).

4. The rivulet width approaches a constant value in the z direction (the solution for the approach is given by Anand and Bejan, 1986).
5. The large majority of flow is confined to an inner region of the rivulet (within the region of width W_i in Figure 2).
6. The inner region is broadened by wetting at the wall (bounded by the outer width, W_o, as shown in figure 2).
7. No flow occurs in this outer region.
8. Since no flow occurs in the outer region, the contact angle is characterized by the static fluid-wall contact angle (α in Figures 2 and 3).

Although the assumption that $W_i >> \delta$, where δ is the channel aperture width, might reasonably be imposed *a priori*, as was assumed by McCreery and McEligot, 2004, the data indicate that this assumption would be overly restrictive.

For laminar flow the shear stress τ is equal to,

$$\tau = \mu \frac{dV}{dy}, \qquad (1)$$

where μ is the dynamic viscosity, $V(y)$ is the fluid velocity in the vertical downward (-z) direction and y is the direction normal to wall. The laminar (Poiseuille flow) velocity profile for flow between parallel walls is given by (Anand and Bejan, 1986),

$$V = \frac{3}{2}\overline{V}(1-\left(\frac{y}{\delta/2}\right)^2), \qquad (2)$$

where $\overline{V}$ is the bulk velocity given by,

$$\overline{V} = \frac{Q}{W_i \delta}, \qquad (3)$$

and where Q is the flow rate in the rivulet. The shear force (F) per unit z length is equal to the gravitational force per unit z length,

$$dF/dz = 2\tau W_i = \rho g W_i \delta, \qquad (4)$$

where, ρ is the fluid density and g is the acceleration due to gravity.
    Using the velocity profile to solve for the shear stress at the walls yields

$$\tau = \mu \frac{dV}{dy} = \frac{6\mu\overline{V}}{\delta}, \qquad (5)$$

and the bulk velocity is given by

$$\overline{V} = \frac{g\delta^2}{12\nu}, \qquad (6)$$

where ν is the kinematic viscosity ($\nu = \mu/\rho$).
    Substitution of the expression for V given in equation (3) into equation (6) leads to the expression

$$W_i = \frac{12Q\nu}{g\delta^3} \qquad (7)$$

5

for the rivulet inner width as a function of flow rate, aperture spacing, and fluid viscosity. This equation may be expressed as a non-dimensional width,

$$\frac{W_i g \delta^3}{Q \nu} = 12 \qquad (8)$$

The Reynolds number (Re) is given by

$$\text{Re} = \frac{V D_h}{\nu} = \frac{2Q}{\nu W_i}. \qquad (9)$$

With equation (7) substituted for W_i, this becomes,

$$\text{Re} = \frac{g \delta^3}{6 \nu^2}, \qquad (10)$$

where the hydraulic diameter (D_h) is given by

$$D_h = \frac{4A}{P_{wetted}} = 2\delta. \qquad (11)$$

Here, A is cross-section flow area and P_{wetted} is wetted perimeter. It is assumed that A and P_{wetted} apply only to flow bounded by W_i and δ, since the flowing liquid is assumed to be confined to this region.

For any given aperture spacing, δ, the model predicts that both the rivulet velocity and the Reynolds number based on D_h, as defined above, are constant, and W_i varies linearly with the flow rate.

2.2 Rivulet width broadening due to wall wetting

The rivulet inner width is broadened near the walls by the fluid wetting the walls. The trigonometric solution for width broadening (shown in Figures 2 and 3), under the assumption of a constant radius of curvature, is given by the expression,

$$W_o = W_i + 2((\delta/2)(1 - \sin(\alpha))/\cos(\alpha)), \qquad (12)$$

where α is the fluid-wall contact angle (shown in Figures 6 and 15)

The assumption of a constant radius of curvature is commonly employed to describe the meniscus in a small diameter tube (Vennard, 1963), and it seems reasonable to apply the assumption to a cylindrical meniscus. However, the profile is expected to flatten as the aperture spacing increases. The aperture spacings for these experiments are considerably smaller than the maximum tube diameter given by Vennard (1963) for which the assumption of constant radius is applicable (diameter < 5 mm). Therefore, the assumption of constant radius is expected to apply.

Dividing the flow into an inner region, where the flow is confined, and an outer static region is, of course, a simplification since the velocity will change continuously from the inner region to the boundary. However, it is doubtful that a two-dimensional flow model would produce a more accurate description of the average steady-state rivulet width since the contact angle changes unpredictably with position due to microscopic surface changes (even for very well cleaned plates). The assumption of steady-state is itself a simplification since rivulets are usually

6

observed to wander at least a small amount over time. A full treatment of dynamic laminar (or turbulent) rivulet flow would require a three-dimensional solution of the transient Navier-Stokes equations, with consideration of dynamic contact angles and contact angle hysteresis effects. Although this approach would give considerable insight into the physics of rivulet flow, it is well beyond our objective of providing a simple and reasonably accurate analytical tool.

3. Experimental method

Experiments were conducted to characterize rivulet flow between two vertically oriented parallel glass plates with dimensions of 30.5 cm by 14 cm using the apparatus shown in Figures 4 and 5. The aperture spacing was set by clamping shims between the two glass plates as shown in Figure 5. The average aperture spacings used in these experiments were 0.168 mm, 0.419 mm, 0.597 mm, and 0.902 mm. The variation of these values was approximately $\pm$ 0.012 mm. (This variation was determined by use of feeler gages, which have thickness tolerances of approximately $\pm$ 0.005 mm). The rivulet inner and outer widths (W_i and W_o, in Figure 2) were measured as a function of flow rate for several fluids: water, water plus wetting agent (8 parts Kodak PhotoFlo per 10,000 parts water), ethyl alcohol, and mineral oil. Relevant fluid properties at the operating temperature of 21 ^{o}C $\pm$ 1 ^{o}C are listed in Table 1. Flow was delivered by a KDScientific model 100 syringe pump with a maximum flow rate of 557 ml/hr, a digital readout resolution of 0.1 ml/hr, and an uncertainty of approximately $\pm$ 1 % of input flow rate (after calibration). Solitary rivulets were generated at the same initial position by feeding fluid to a wedge shaped piece of porous material (coffee filter paper) inserted between the two plates. It was necessary to wrap the wick material around the inlet tube. Otherwise, entrainment of small air bubbles was observed to occur during several unsuccessful experiments. The consequence of air bubbles was to destabilize the flow and cause either oscillations or, in experiments that employed the largest aperture spacing used (0.902 mm average), meandering rivulet flow. The glass plates were cleaned carefully before each experiment using first acetone and then ethyl alcohol.

The rivulets were observed to contract in width below the injection point (due to fluid acceleration by gravity) and then approach an approximately constant width as the terminal velocity was approached. The average width was measured from digital images taken of an area, approximately 20 cm below the entrance, where the rivulets appeared to have reached their terminal velocity. This position provided rivulet development lengths of greater than 125 hydraulic diameters, which was sufficient to insure well-developed flow. The distance from the measurement position to the channel exit (approximately 10 cm) was sufficient to insure that exit effects did not disturb upstream flow in the measurement region. The measurement area imaged by the camera was typically 19.60 mm by 14.90 mm. For experiments that employed the minimum aperture width (0.168 mm) porous sponge material was placed at the channel exit to wick away liquid and prevent the formation of a liquid column above the exit held in place by capillary forces. Experiments that employed larger aperture widths drained freely and wicking at the channel exit was not necessary.

The boundaries of the inner rivulet are prominently visible as dark lines in images due to the effects of refraction and total internal reflection at the fluid-air interfaces, as shown in Figures 5 and 6. The outer rivulet boundary was not visible unless the additional technique of interposing a black mask between the diffuse light source and rivulet boundary was used, also shown in

Figures 5 and 6. The mask was manually placed in a position such that white light was refracted to the camera inside the rivulet boundary, which contrasted with the black mask immediately outside the rivulet boundary. Although dye mixed in the fluid made the outer boundary marginally more visible, the dye decreased the contrast of the inner boundary and was therefore not used for the majority of experiments. Use of collimated light rather than diffused light increased the contrast of the inner width boundary but decreased the visibility of the outer boundary. The best compromise was to use diffuse light with the diffuser placed approximately 20 cm behind the channel.

The average rivulet inner width, W_i, shown in Figures 4 and 5, was measured by either of two procedures: For rivulets where the width did not vary significantly with vertical position, the inner pixel width was measured directly at typically five locations and the results were averaged. The average pixel width was then divided by a calibration constant (75.59 pixels/mm for these experiments) to determine the width.

For rivulets with profiles that varied with position, such as the rivulet shown in Figure 6, the following method was used:
1. Transform the image to a black and white image in Photoshop Elements 2.0 (Adobe, 2002).
2. Select the inner boundary using the Photoshop "magic lasso" tool.
3. Color the area within the inner width black.
4. Measure the number of black pixels using ImageJ software (Rasband, 2003).
5. Divide the number of black pixels by the pixel length of the image of the rivulet. The result is the average inner width of the rivulet in pixels.
6. Divide the pixel width by the calibration length (= 75.6 pixels/mm for these experiments).
7. The result is the average rivulet width in millimeters

The outer width, W_o, was determined by measuring the average difference between the outer width boundary position and the inner width position on one side of the rivulet (the side at which a mask was used to make the outer boundary visible, as shown in Figures 6 and 7). Twice the average difference was then added to the inner width to specify the outer width.

4. Experiment uncertainties

The experimental results are subject to a number of sources of uncertainty. We believe that the four most important sources of uncertainty are, in order, the aperture spacing, the resolution of the rivulet boundaries in the images, the parallax of viewing an off-center image of a rivulet, and the static contact angle. Uncertainties in the resolution of rivulet boundaries and uncertainty due to parallax result in rivulet width measurement uncertainty and uncertainty in the Reynolds number calculated from Equation 9. Uncertainty in the measured aperture spacing results in uncertainties in in the values predicted for W_i and W_o, and in Reynolds number calculated from Equation 10. Uncertainty of the measured contact angle results in uncertainty in the prediction of W_o. The aperture spacing was set by clamping shims, with a tolerance of approximately ± 0.005 mm, between glass plates. The aperture spacing was measured using feeler gauges with a stated manufacturing tolerance of ± 0.005 mm. The variation of the measured aperture spacing around the mean was approximately ± 0.012 mm. Predicted inner rivulet widths, using the upper and lower limits of the aperture spacing, are shown in Figures 8 through 13. Although this variation in measured aperture spacing is small, it had a large effect on predicted values of the rivulet width for the smallest average aperture spacing of 0.168 mm, since it enters the prediction to the third power.

The pixel resolution from the digital images was approximately three pixels, with an object resolution of 75.59 pixels/mm. The measurement uncertainty in the rivulet widths due to pixel resolution was therefore approximately $\pm$ 0.04 mm. The uncertainty of measuring W_o is larger than for W_i since two measurements are added together to determine this width. The uncertainty is therefore approximately the square root of two times the uncertainty for W_i, or, approximately $\pm$ 0.06 mm. Error bars are shown in the two figures (Figure 11 and 13) where the uncertainty values for W_i and W_o exceed the vertical widths of the symbols.

An additional uncertainty of measuring W_i resulted from the parallax between the near and far walls of the channel for an off-center rivulet. Parallax was minimized by placing the camera lens approximately 40 cm from the flow cell and using the maximum focal length available on the zoom lens (84 mm). The angular field of view was thereby reduced to approximately 3^0. The concave fluid surfaces bounding W_i also contribute to minimizing parallax error. The maximum uncertainty due to parallax was calculated to be approximately -0.01 mm (parallax error always reduces the measured width) for the largest aperture spacing experiments, and lower, proportional to aperture spacing, for the smaller aperture experiments.

The maximum RMS uncertainty in measured W_i is a combination of pixel resolution and parallax uncertainties, and varied from approximately $\pm$ 0.04 mm for the smallest aperture spacing to approximately $\pm$ 0.045 mm for the largest aperture spacing. The relative uncertainty of measured W_i (= uncertainty/W_i) varied from approximately $\pm 7\%$ at the highest flow rates to $\pm 30\%$ at the lowest flow rates. Exceptions are for the experiments that used water or water plus wetting agent for flow through the largest aperture, with spacing of 0.902 mm. For those experiments the relative uncertainty varied from approximately $\pm 15\%$ at the highest flow rates to $\pm 65\%$ at the lowest flow rates.

The uncertainty of predicted W_i, from Equation 7 is dominated by the uncertainty of the measured aperture spacing. The relative uncertainty of calculated W_i is therefore equal to three times the relative uncertainty of the measured aperture spacing = 0.075 mm/ aperture spacing.

The relative uncertainties in predicted W_i, corresponding to the average aperture spacings used in these experiments of 0.168 mm, 0.419 mm, 0.597 mm, and 0.902 mm, are respectively, $\pm 45\%$, $\pm 18\%$, $\pm 13\%$, and $\pm 8\%$.

The flow rate uncertainty was approximately $\pm 1\%$ of the input volumetric flow rate.

The uncertainty in the Reynolds number, calculated from Equation 9, using measured values of W_i, is dominated by the uncertainty of measured W_i. The relative uncertainty of the Reynolds number, using measured values of W_i, is therefore approximately equal to that of W_i, as described above.

The uncertainty of the predicted Reynolds number, calculated from Equation 10 is dominated by the uncertainty of the measured aperture spacing. The relative uncertainty in calculated Reynolds number is therefore approximately the same as for W_i calculated from Equation 7 using the measured aperture spacing, as described above.

The $\pm 1\%$ uncertainty in measured contact angle results in an uncertainty in the difference between W_o and W_i of approximately $\pm 3\%$ of the aperture spacing, or a maximum of approximately 0.03 mm for the largest aperture spacing (0.902 mm).

The uncertainty in calculating W_o from Equation 10, using average measured aperture spacing, is due to uncertainty in calculated W_i, which is in turn due to uncertainty in both the aperture spacing as described above, and contact angle. The RMS relative uncertainties in calculated W_o, corresponding to the average aperture spacings used in these experiments of 0.168 mm, 0.419 mm, 0.597 mm, and 0.902 mm, are, $\pm 48\%$, $\pm 19\%$, $\pm 14\%$, and $\pm 8\%$, respectively.

5. Experimental results and comparisons with calculations

In this section the data are compared with predictions using the analytical model. Comparisons of measured inner and outer rivulet widths as a function of flow rate with predicted values are shown in Figures 8 through 13, for each combination of fluid and aperture spacing. The calculations of W_i (Equation 7) used measured flow rates and aperture spacings. The calculated valued of W_i are presented as two lines in each graph, one representing the aperture spacing at minimum tolerance and one at maximum tolerance. Predicted values of W_o used the average measured aperture spacing and measured contact angle in Equation 12.

Predicted values for the inner rivulet width, W_i, agreed very well with measured values and were, in general, within the estimated experimental uncertainties. Most exceptions were for very low flow rates where the measured inner width W_i tended to be larger than predicted for flow rates near the drop flow limit. This underprediction of W_i is seen most clearly in the Reynolds number versus flow rate plot (Figure 14) where the Reynolds number, using the measured W_i in equation 9, deviates from the constant predicted values at low flow rates. The approximately linear relationship between W_i and flow rate was maintained for W_i considerably smaller than the aperture spacing for all of these experiments, except for the experiment which employed the minimum aperture spacing (0.168 mm average). It might be expected that the deviation from linearity would be a strong function of the non-dimensional inner width ($= W_i / \delta$). However, this strong dependency does not appear to be the case, as may be seen most clearly in Figure 15, which relates the Reynolds number to the non-dimensional inner width. The rivulet-drop flow transition displays considerable hysteresis as a function of the change in flow rate with time.

Hysteresis was not investigated in any detail, except to note that rivulet flow may be maintained at a lower flow rate for decreasing flow rates than for increasing flow rates. One reason may be that, for decreasing flow rates, the residual lubrication film deposited by successive drops is wider and thicker than for increasing flow rates.

Predicted values of the outer rivulet width agree reasonably well with experimental results (to within approximately $\pm 20\%$). Predicted values of W_o were based on the average measured aperture spacing. The outer width is more difficult to measure than the inner width, and its uncertainty is correspondingly larger The uncertainty in the measured static contact angle is approximately $\pm 1^0$, which resulted in an uncertainty in the predicted rivulet width broadening of approximately $\pm 3\%$ of the aperture spacing for the range of contact angles measured. Contact line dynamics may also contribute to this uncertainty since the effective contact angle is know to vary considerably with the direction of motion and velocity of the contact line. Advancing contact lines usually have a contact angle that is larger than the static contact angle and receding contact lines typically have a contact angle that is smaller than the static contact angle (Hewitt *et. al.,* 1982). Although the assumption of a static rivulet boundary is accurate for some cases, the rivulet boundaries were observed to move slowly in other cases.

The meandering flow limit was investigated by Anand and Bejan (1986). According to their Reynolds number criterion, meandering flow is achieved when the Reynolds number based on the aperture spacing (δ) (rather than on the hydraulic diameter, which we use) approaches 2100. The maximum Reynolds number for our experiments was approximately 1400, based on the hydraulic diameter (approximately 700 based on the aperture spacing). Consistent with Anand and Bejan's (1986) results, we did not observe meandering flow (which they defined as deviations in the direction of the rivulet trajectory greater than 30° from vertical). Another flow regime limit must exist when the aperture spacing is too large to maintain a rivulet attached to both walls. Rivulet flow should then be observed attached to one or the other wall, or as separate rivulets attached to both walls. However, this regime was not observed in our experiments because the aperture spacing was small and the investigation of other flow regimes was beyond the scope of our investigation.

6. Concluding Remarks

Experiments were performed to measure rivulet widths for flow in parallel-wall channels with aperture spacing ranging from 0.152 mm to 0.914 mm. The results of experiments with water, water plus wetting agent, ethanol, and mineral oil were compared with a simple steady-state laminar flow model The various fluids provided a fairly wide range of properties to test the analytical model. The various aperture spacings and fluids employed provided a range of rivulet Reynolds numbers ranging from approximately 5 to 1400. Predicted values of the inner rivulet width, W_i, agreed very well with measured values and were mostly within experimental uncertainty. For any given aperture spacing, the analysis and data showed that both the rivulet velocity and Reynolds number based on hydraulic diameter are approximately constant and that W_i varies approximately linearly with flow rate. The predicted outer rivulet width agreed reasonably well with experimental results (to within approximately $\pm 20\%$). Some uncertainty in measuring the outer width is attributed to the difficulty of measuring it in comparison with the inner width. Contact line dynamics may also have contributed to this uncertainty since the effective contact angle is known to vary considerably due to motion of the contact line. The

analytical model appears to be valid for a wider range of fluid properties and aperture spacings than were tested in the reported experiments. It remains for future research to define these limits, to characterize the transitions from rivulet flow to other flow regimes, and to extend these initial results to flows in channels with more complex geometry, such as geological fractures.

Acknowledgment

References

Adobe Systems Inc., 2002, Photoshop Elements 2.0.

Anand, A., Bejan, A., 1986. Transition to meandering rivulet flow in vertical parallel-plate channels. J. Fluids Engineering 108, 269-272.

Bentwitch, M., Glasser, D., Kern, J., Williams, D., 1976. Analysis of rectilinear rivulet flow. AIChE Journal 22, 772-778.

Hewitt, G.F., Delhaye, J.M., Zuber, N., 1982. Multiphase science and technology, Volume 1, Hemesphere, New York.

Hartley, D.E., Murgatroyd, W., 1964. Criteria for the break-up of thin liquid layers flowing isothermally over solid surfaces. Int. J. Heat and Mass Transfer 7,. 1003-1015.

Hughes, D.T., Bott, T.R. 1998. Minimum thickness of a liquid film flowing down a vertical tube. Int. J. Heat Mass Transfer 41, 253-260.

Johnson, M.F.G., Schluter, R.A., Miksis, M.J., Bankoff, S.G., 1999. Experimental study of rivulet formation on an inclined plate by fluorescent imaging. J. Fluid Mech. 394, 339-354.

McCreery, G.E., McEligot, D.M., 2004. "Transition to Meandering Rivulet Flow in Vertical Parallel-Plate Channels", accepted for publication, ASME J. Fluids Engineering, vol. 126.

McCreery, G.E., Larson, T.K., Condie, K.G., 1989. Once through steam generator AFW flow distribution and heat transfer. Hassan, Y.A., editor, Thermal hydraulics of nuclear steam generators/heat exchangers. ASME HTD 102, 7-20.

Mikielewicz, J., Moszynski, J.R., 1976. Minimum thickness of a liquid film flowing vertically down a solid surface. Int. J. Heat Mass Transfer 19, 771-776.

Nicholl, M.J., Glass, R.J., Wheatcraft, S.W., 1994. Gravity-driven infiltration instability in initially dry nonhorizontal fractures. Water Resources Research 30, 2533-2546.

Orr, B., Thomson, E., Budwig, R., 1997. Drakeol #5 thermophysical property measurements. University of Idaho Mechanical Engineering Department report, 12-18-97.

Rasband, W., 2003. ImageJ 1.29x software. National Institutes of Health, Washington, DC.

Su, G.W., Geller, J.T., Preuss, K., Hunt, J.R., 2001. Solute transport along preferential flow pathways in unsaturated fractures. Water Resources Research 37, 2481-2491.

Schmuki, P., Laso, M., 1990. On the stability of rivulet flow. J. Fluid Mech. 215, 125-143.

Young, G.W., Davis, S.H., 1987. Rivulet instabilities. J. Fluid Mech. 176, 1-31.

Towell, G.D., Rothfeld, L.B., 1966. Hydrodynamics of rivulet flow. AIChE Journal 12, 972-980.

Vennard, J.K., 1963. Elementary fluid mechanics, John Wiley and Sons, New York.

Weast, R.C., 1971. CRC handbook of chemistry and physics 52nd Edition, The Chemical and Rubber Company, Cleveland, Ohio.

Table 1. Fluid properties[1] and static glass-fluid contact angle[2] at temperature = 21 °C

	Density (Kg/m^3)	Kinematic viscosity (m^2/s)	Static contact angle ($\pm 1^0$)
Water	998	0.98x10^{-6}	15
Water plus Wetting agent (1 part/ 8,000)	998	0.98x10^{-6}	11
Mineral oil	835 $\pm$ 2	1.42x10^{-5} $\pm$ 0.03x10^{-5}	7
Ethyl alcohol	789	1.18x10^{-6}	5

---

[1] Fluid properties are from Weast, 1971, and, for mineral oil, Orr, Thomson, Budwig, 1997.
[2] Contact angle measurements were obtained using an FTA200 contact angle analyzer, First Ten Angstroms, Inc.

Figures
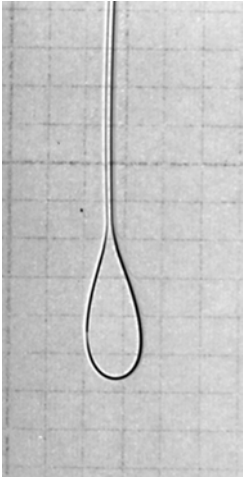
Figure 1. Water drop with trailing rivulet.
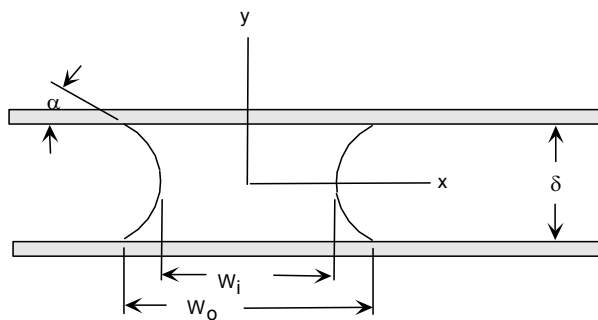
Figure 2. Rivulet cross-section nomenclature.
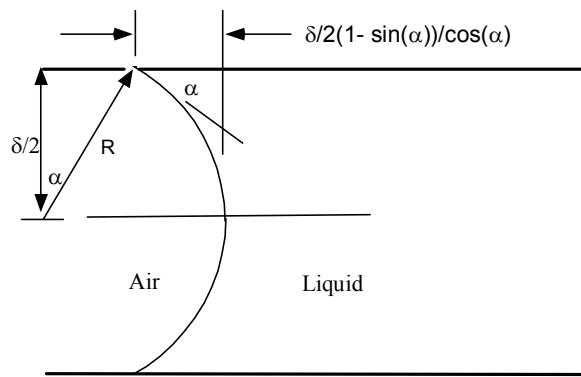
Figue 3. Rivulet width broadening due to wall contact angle (α).
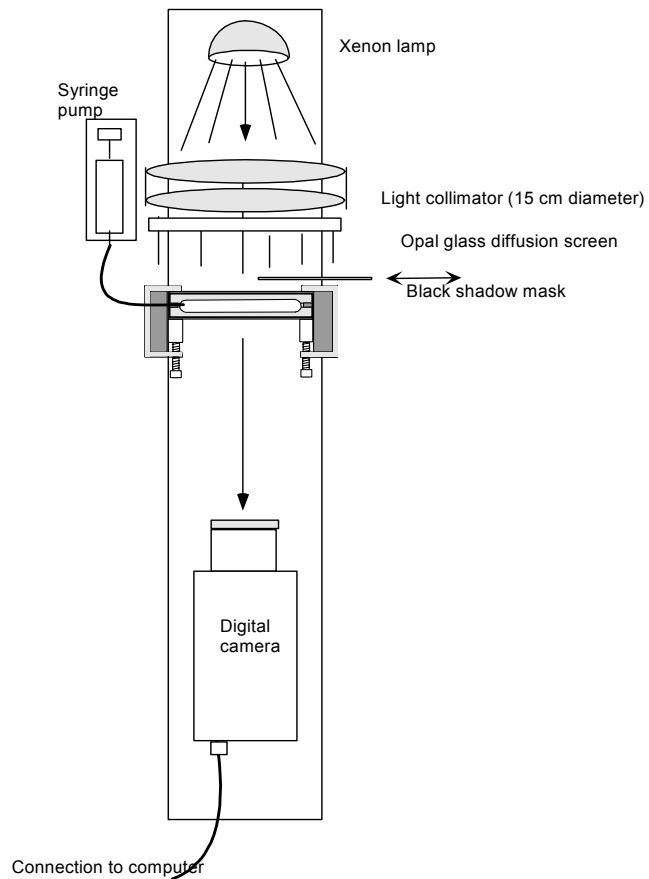
Figure 4. Top view of apparatus.
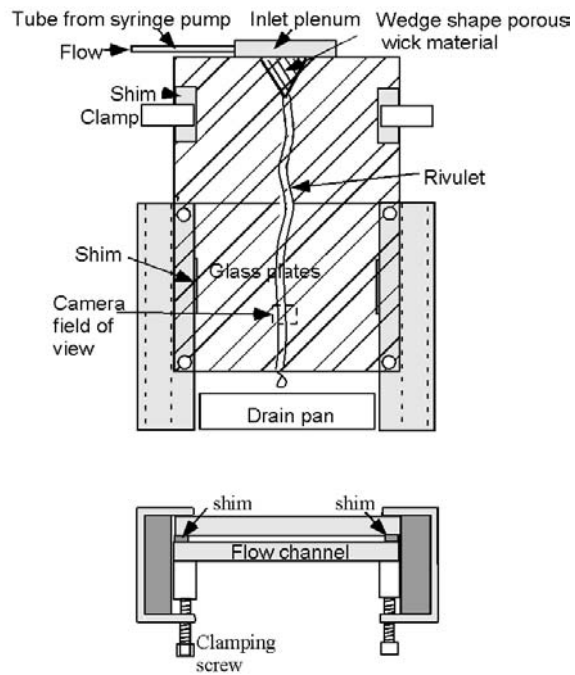
Figure 5.   Top and side-view of flow channel.
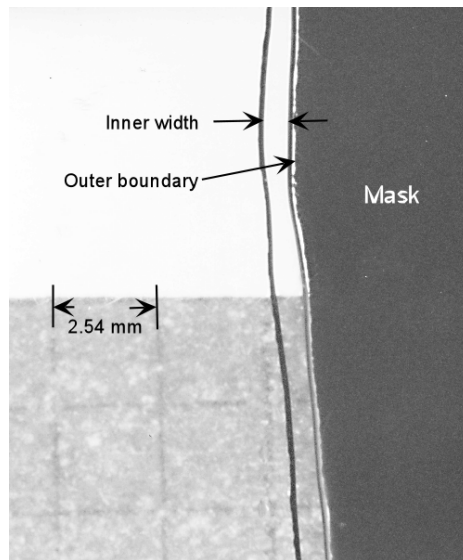
Figure 6. Photograph of rivulet.
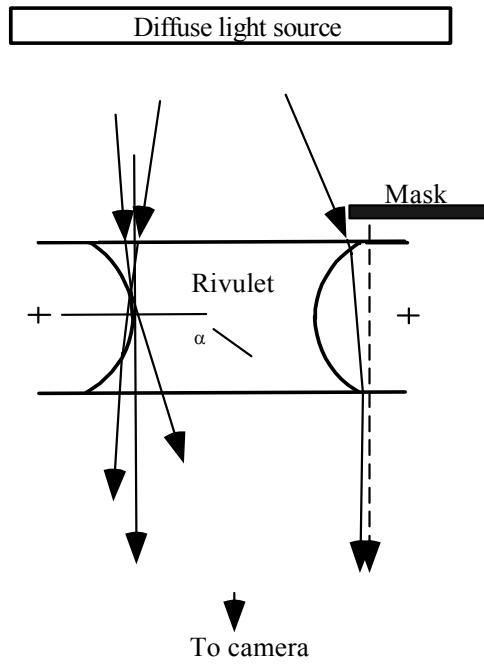
Figure 7. Light paths through rivulet.
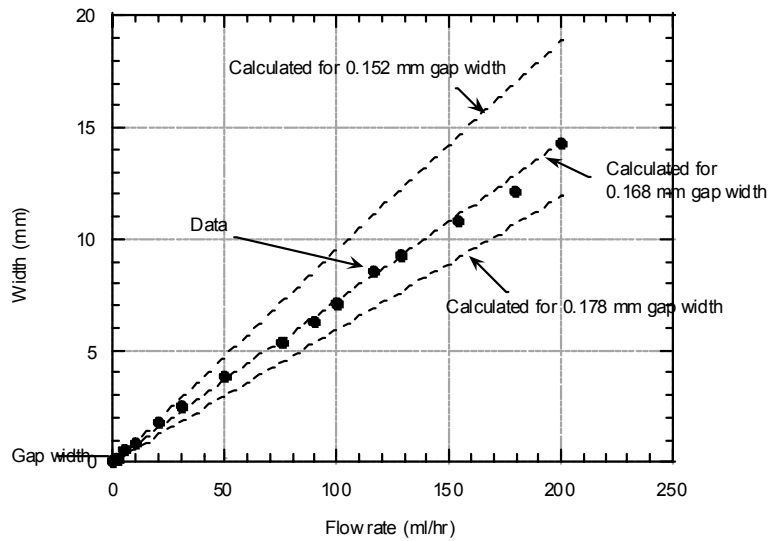
Figure 8. Comparison of predicted and measured water rivulet flow width for 0.168 mm average aperture spacing (W_o was indistinguishable from W_i in this experiment).
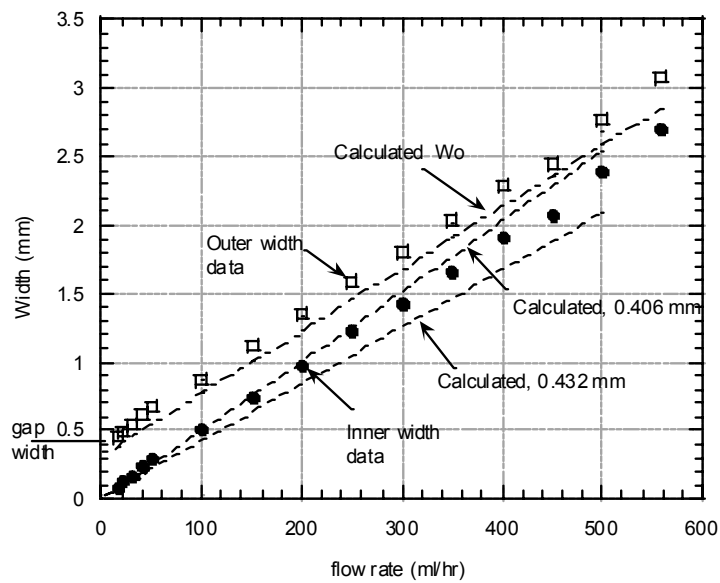
Figure 9. Comparison of predicted and measured water rivulet flow width for 0.419 mm average aperture spacing.
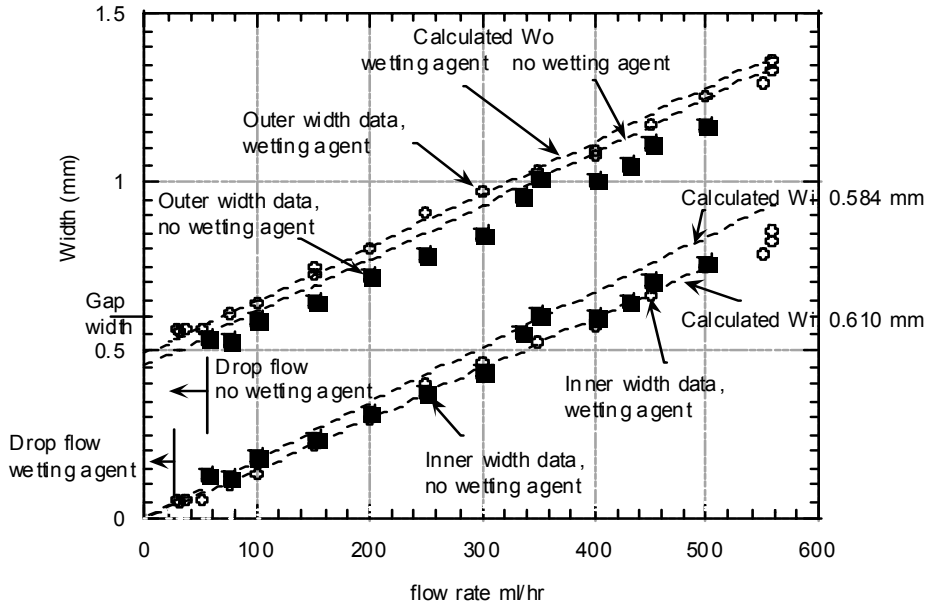
Figure 10. Comparison of predicted and measured water and water plus wetting agent rivulet flow widths for 0.597 mm average aperture spacing .
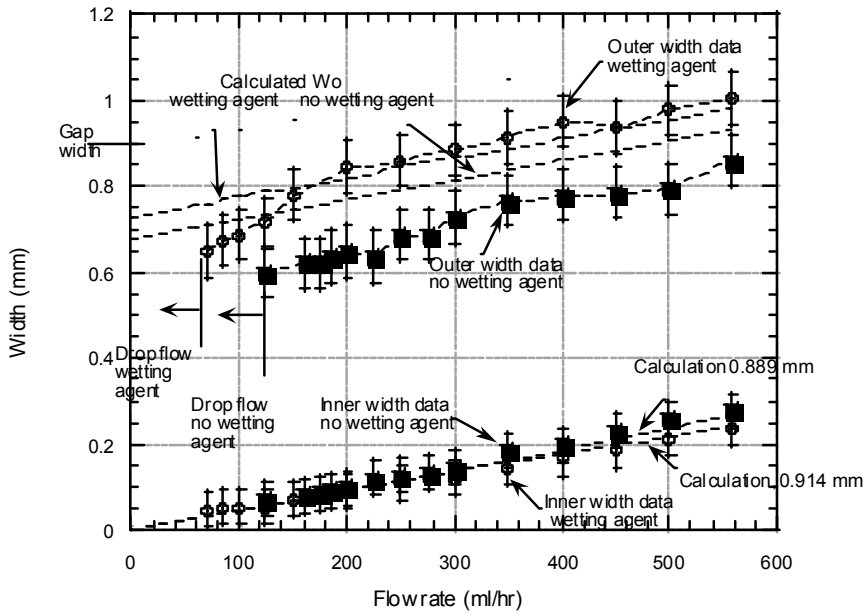
Figure 11. Comparison of predicted and measured water and water plus wetting agent rivulet flow widths for 0.902 mm average aperture spacing.

20
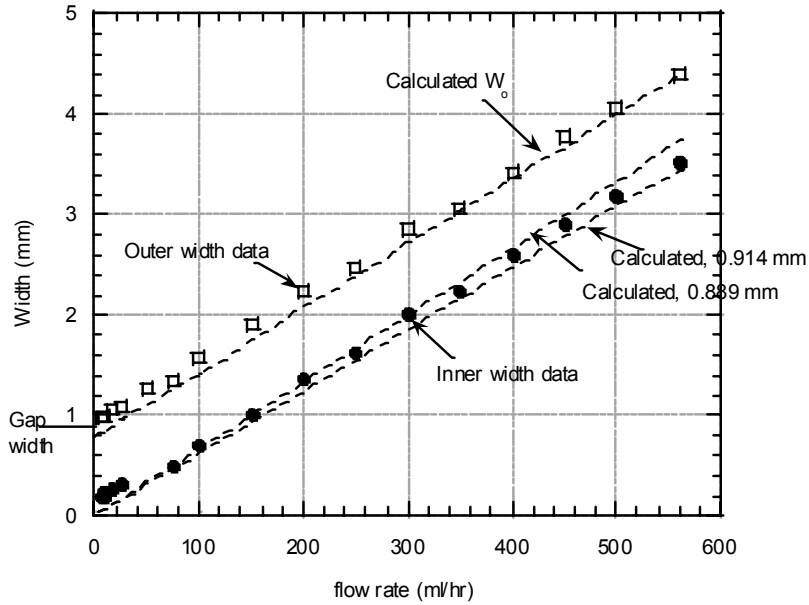
Figure 12. Comparison of predicted and measured mineral oil rivulet flow width for 0.902 mm average aperture spacing.
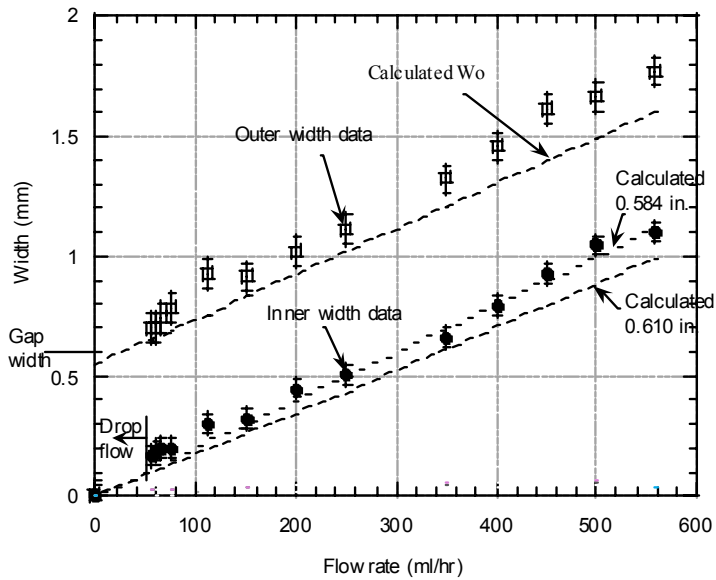
Figure 13. Comparison of predicted and measured ethanol rivulet flow width for 0.597 mm average aperture spacing.
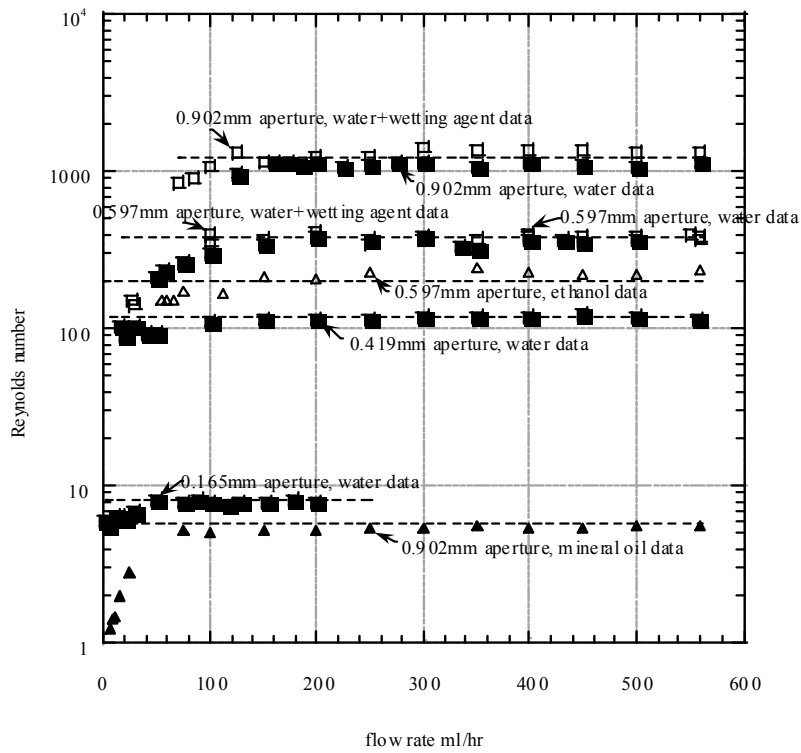
Figure 14. Comparison of Reynolds number calculated from Equation 8 using measured values of W_i and predicted from Equation 9 (the dashed lines).
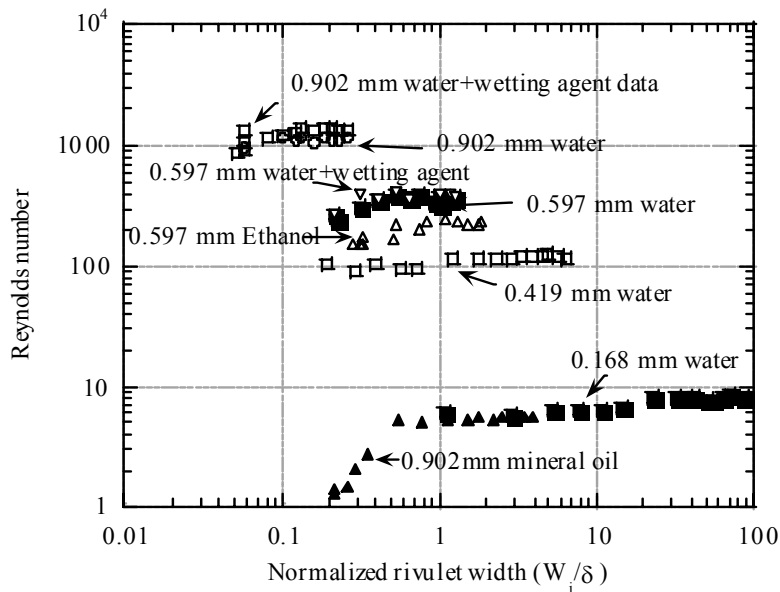
Figure 15. Reynolds number calculated from Equation 8, using measured values of W_i as a function of normalized aperture spacing.

APPENDIX A

Solution for full-width laminar parabolic velocity distribution

The solution approach is to assume that velocity, V, is a function of y over the total rivulet width rather than assume that flow is confined to the inner width as for the simplified solution. The steady-state force balance, shear force = gravitational force, is then,

$$dF/dz = 2\tau W_o = \rho g A \tag{A1}$$

where, A = cross-section area of the rivulet,

$$A = W_i \delta + \delta^2 \left[\frac{1-\sin\alpha}{\cos\alpha} + \frac{1}{2}\tan(\alpha) - \frac{(\pi/2-\alpha)}{2\cos^2\alpha} \right] \tag{}$$

For a laminar parabolic velocity distribution the shear stress at the wall is,

$$\tau_{wall} = \frac{4\mu V_{max}}{\delta} \tag{A2}$$

where, V_{max} = maximum velocity (at y = 0)

Substituting A2 into A1 and solving for flow rate $Q = \bar{V}A$ yields,

$$Q = \frac{g\delta A^2}{8\nu\left(\frac{V_{max}}{\bar{V}}\right)\left[W_i + \frac{\delta}{2}\frac{1-\sin(\alpha)}{\cos(\alpha)} \right]} \tag{A3}$$

Where, $\bar{V}$ = average velocity $= Q/A = 1/A\int_A V(y)dA$ (A4)

(The simplified solution is $Q = \bar{V}W_i\delta = (2/3)V_{max}W_i\delta$)

Then next step is to solve for $\bar{V}$. The integral in A4 is most easily evaluated and expressed by considering a ¼ cross-section of the rivulet and using normalized dimensions, as shown in Figure A1,

y' $= y/(\delta/2)$

x' $= x/(\delta/2)$

V'(y) = V(y)/V_{max} = (1-y'^{2})

W_i' = normalized inner half-width = $(W_i/2)/(\delta/2)$

W_o' = normalized outer half-width = $(W_i/2)/(\delta/2)$

The normalized cross-section area for the ¼ rivulet is,

$$A' = W_i' + \frac{1-\sin(\alpha)}{\cos(\alpha)} + \frac{1}{2}\tan(\alpha) - \frac{\pi/2-\alpha}{2\cos^2(\alpha)} \tag{A5}$$

Using cylindrical co-ordinates, the integral of V'dA' for the section between W_i' and W_o' is,

$$\int_0^1 (1-y'^2)dA' = R'^4 \int_0^b (a-\sin^2(\theta))(1-\cos(\theta))\cos(\theta)d\theta$$
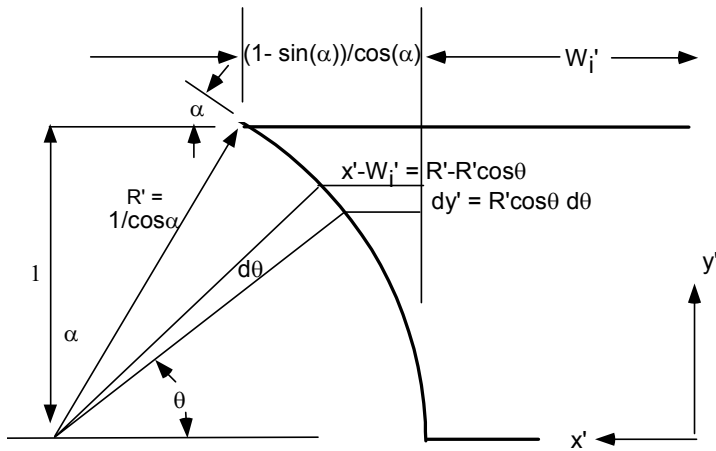
Figure A1. Cylindrical non-dimensional coordinates.

where,

$a = 1/R'^2$

$R' = \dfrac{1}{\cos(\alpha)}$

$b = \dfrac{\pi}{2} - \alpha$

The solution for normalized average velocity as a function of W_i' and α is,

$$\bar{V}' = \left(\frac{1}{A'}\right)\left[\left(W_i'\frac{2}{3}\right) + R'^4 \left(a\cdot\sin(b) - \frac{1}{2}\cos(b)\cdot\sin(b) - \frac{1}{2}a\cdot b - \frac{1}{3}\sin(b)^3 - \frac{1}{4}\sin(b)\cdot\cos(b)^3\right.\right.$$
$$\left.\left. + \frac{1}{8}\cos(b)\cdot\sin(b) + \frac{1}{8}b \right)\right] \tag{A6}$$

The ratio of flow rate, as a function of W_i' and α, divided by the flow rate for the simplified solution,

24

$$Q_{simplified} = \frac{g\delta^3}{12\nu} W_i \tag{A7}$$

is solved by dividing A3 by A7, non-dimensionalizing, and substituting A5 into the resulting equation to arrive at,

$$Qratio = \frac{Q}{Qsimplified} = \left[W_i' + \frac{1-\sin(\alpha)}{\cos(\alpha)} + \frac{1}{2}\tan(\alpha) - \frac{\pi/2-\alpha}{2\cos(\alpha)} \right]^2 \frac{(\frac{3}{2})\overline{V}'}{(W_i' + \frac{1/2(1-\sin(\alpha))}{\cos(\alpha)})W_i'}$$

$$\tag{A8}$$

In the limit of $W_i' \gg 1$, $\overline{V}' = \frac{2}{3}$ (the same as for the simplified solution), and $Q_{ratio} = 1$.

APPENDIX B. Numerical model

A steady laminar flow model for a rivulet was formulated using the finite-element code FlexPDE (PDE Solutions, Inc., 2005). FlexPDE is a general partial differential equation solver that uses the finite element method for numerical solutions of boundary value problems. Flow was assumed to be confined to a half-rivulet geometry with a given contact angle and semi-circular liquid-air interface. The geometry was three-dimensional with flow driven by input inlet and outlet pressures. The equivalent pressure difference for steady-state rivulet flow with gravity force balanced by wall shear force is $\Delta P = \rho g L$, where L is rivulet length in the flow direction. Boundary conditions were zero-slip at the walls and zero-shear at the liquid-air interface and at the symmetry boundary. An example plot of rivulet cross-section isovels for normalized velocities parallel to the rivulet flow direction (Vz/Vz-max) is shown in Figure B1, below. A typical water-glass contact angle of 15° was used. The aspect ratio was, $W_i/\delta = 1.633$.
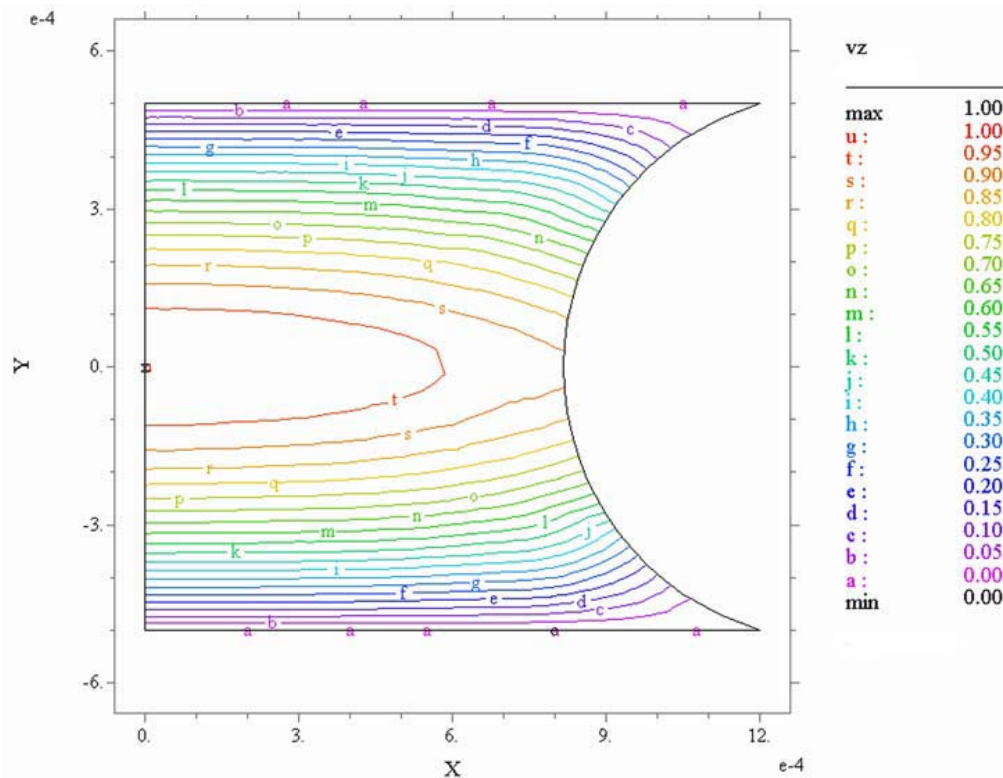
Figure B1. Numerically calculated isovels.

A comparison of numerically calculated flow rate with the simplified model is presented in Figure   for a wetting angle of 15°. The ratio of flow rates for a given aspect ratio is,

$$Qnumerical / Qsimplified = \frac{\int V_z dA}{\left(\dfrac{\rho g \delta^3 W_i}{12 \mu} \right)}$$

Where, A = area normal to flow direction (z).

The flow rate ratio is a function solely of aspect ratio and wetting angle and not fluid properties since, from an examination of the Navier-Stokes equations formulation for this problem, Vz is proportional to ρg and inversely proportional to μ.

A comparison with data shows that both the numerical and simplified solution lie within data uncertainty.   The simplified solution is closer to the numerical solution than the full-width 1D solution for aspect ratios greater than approximately 2.
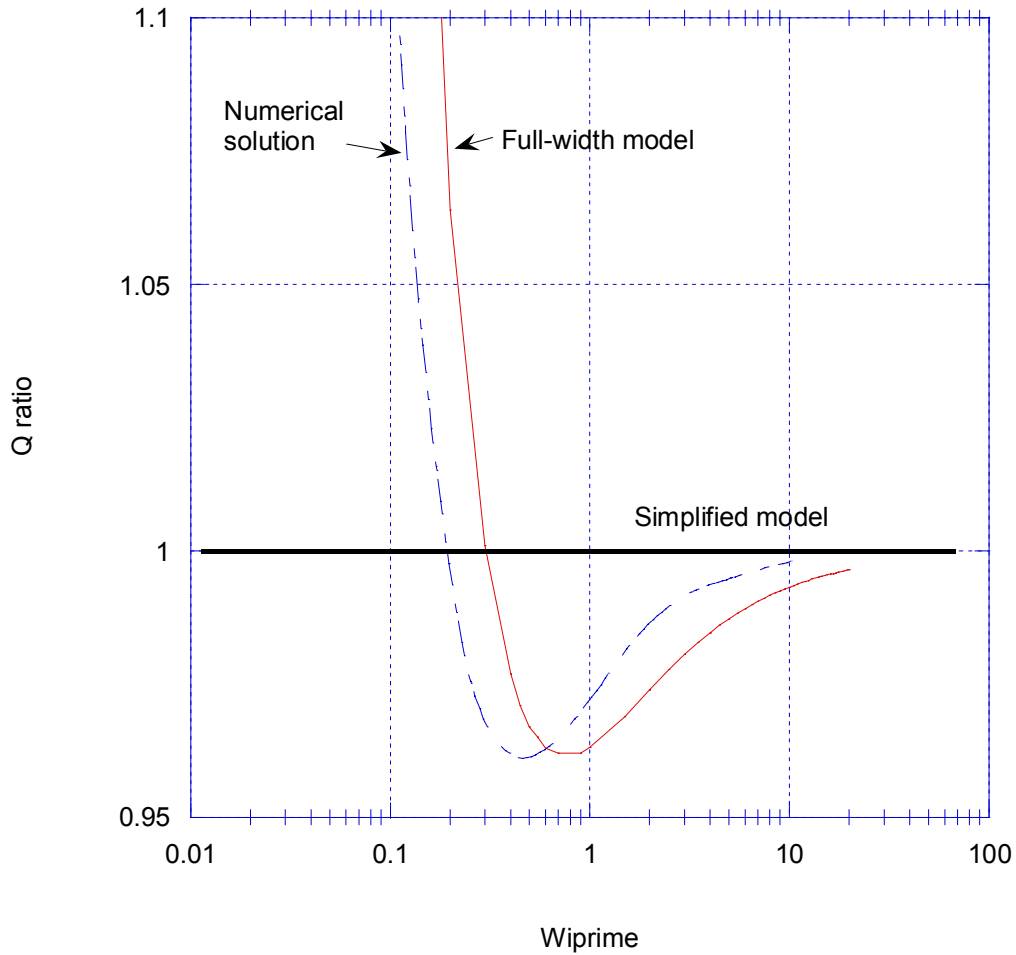
Figure B2. Comparison of numerical and full-width model calculations for a wetting-angle of 15°.

A comparison for wetting angle equal to 5° is shown below. The simplified solution provides a closer comparison with the numerical solution than does the full-width 1D solution for aspect ratios greater than approximately 0.2. A comparison with data shows that both the numerical and simplified solutions lie within data uncertainty. The minimum aspect ratio of data with wetting angle equal to approximately 5° (ethanol data obtained in a channel with average aperture spacing of 0.597 mm) was approximately 0.12.

Reference:
Flex PDE Manual, Version 4.2.10, PDE Solutions, Antioch, California, USA.
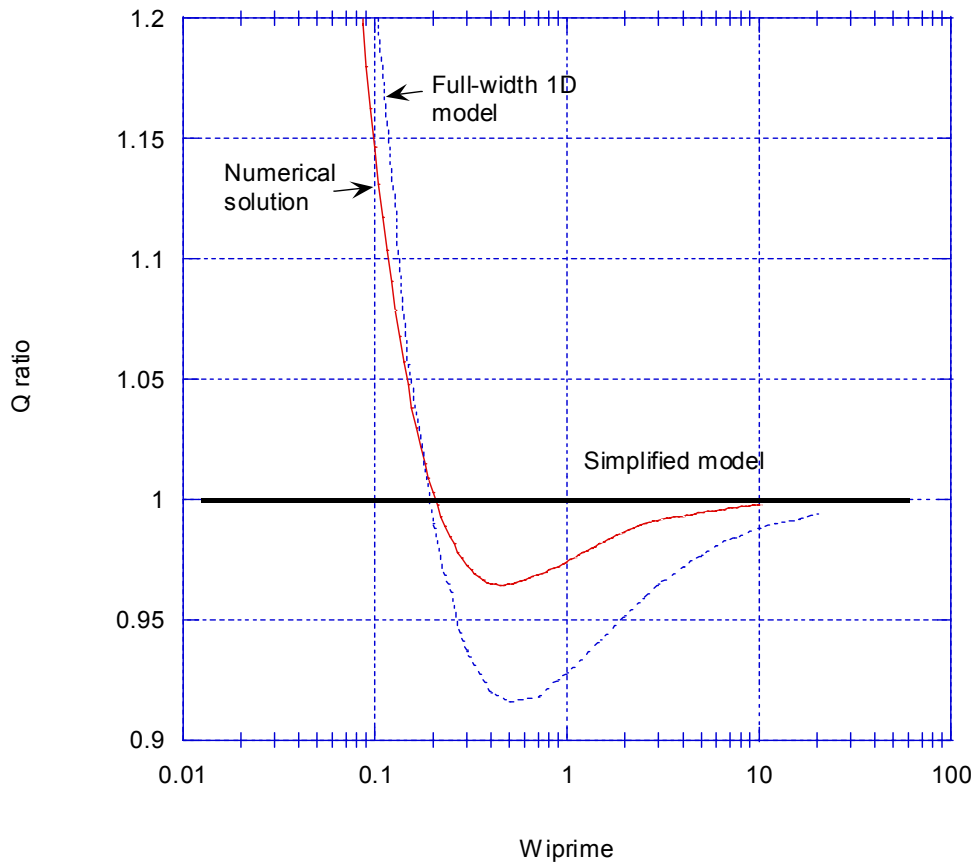
Figure B3. Comparison of numerical and full-width model calculations for a wetting angle of 5°.

APPENDIX C. Non-dimensional plots and associated data table

Figure C1. Non-dimensional width measurements normalized by prediction of simple approach. (Water: circles, $\delta = 0.168$ mm; squares, $\delta = 0.419$ mm; triangles, $\delta = 0.597$ mm; diamonds, $\delta = 0.902$ mm; water with wetting agent: crossed square, $\delta = 0.597$ mm; diagonal-square, $\delta = 0.902$ mm; mineral oil: inverted triangle, $\delta = 0.902$ mm; ethanol: dotted circles, $\delta = 0.597$ mm.)

05-GA50027-16-1

Figure C2. Comparisons between measured Reynolds numbers and those predicted via simple approach (symbols as in Figure C1).

Table C1 continued. Tabulated data for dimensional and non-dimensional inner-widths.

05-GA50027-16-2

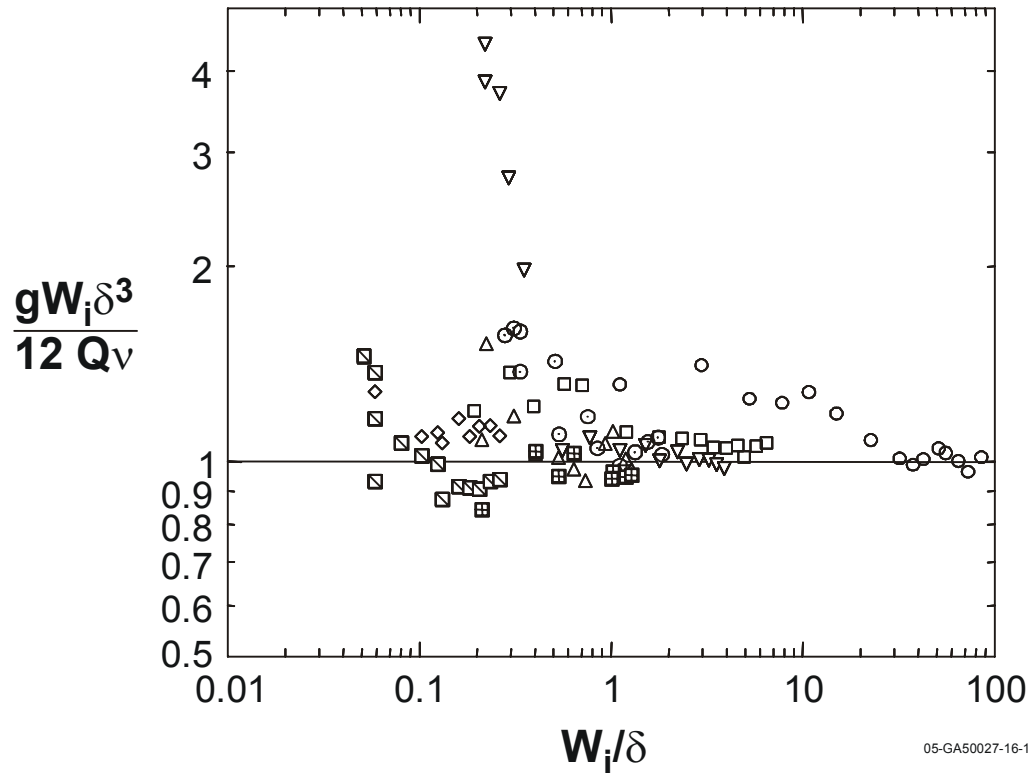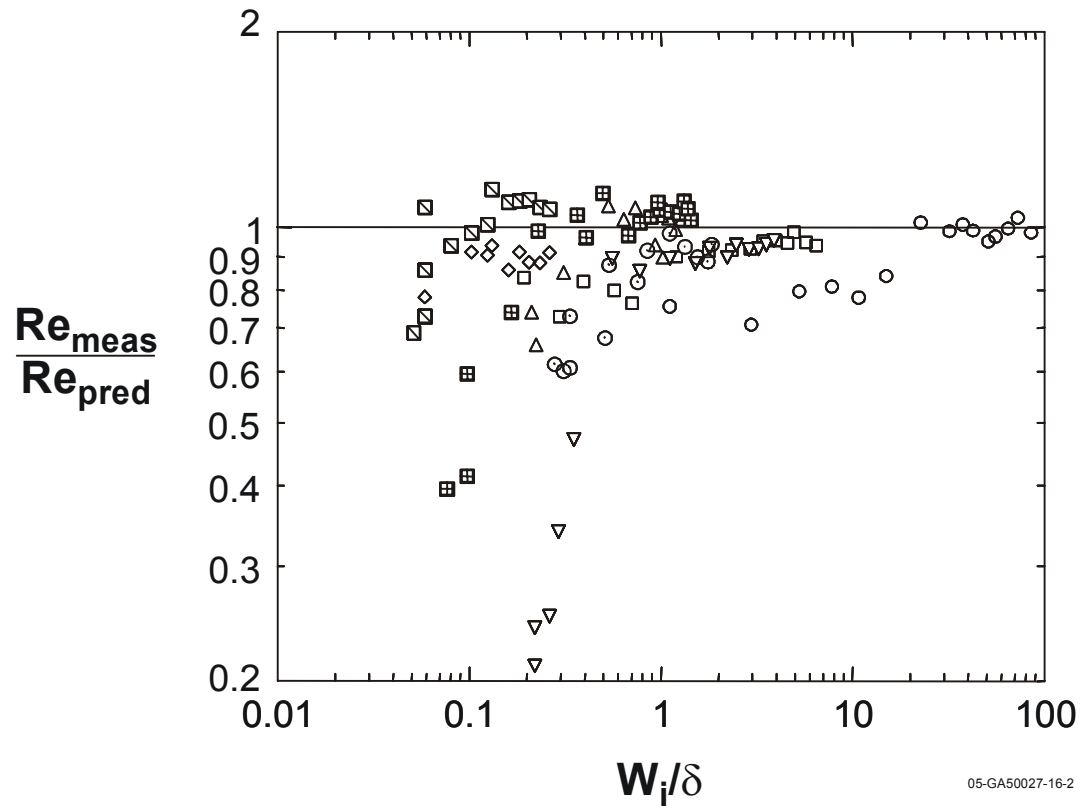| Flow rate (ml/hr)	W 0.17mm	NDW 0.17mm	W 0.42	NDW 0.42	W 0.90 min	NDW 0.90 min	W 0.60 eth	NDW 0.60 eth	W 0.90	NDW 0.90	NDW 0.90 WA	W 0.90 WA	W 0.60	NDW 0.60	W/delta	Re	W 0.60 WA	NDW 0.60 WA
17.5																		
20																	0.097856	15.982
28																	0.076583	11.674
30																	0.097856	12.786
35																	0.097856	
50																214.89		8.9499
56													0.22337	18.24	0.22337	238.24		
75													0.21273	12.971	0.21273	267.93	0.16593	10.117
100																	0.22975	10.506
100.8													0.31059	14.09	0.31059	308.4		
150																	0.3659	11.155
150													0.40419	12.322	0.40419	348.08	0.40844	12.452
200													0.53183	12.16	0.53183	389.9	0.49779	11.382
250													0.63819	11.674	0.63819	372.24	0.67648	12.374
300																	0.77434	11.803
300.5													0.73605	11.201	0.73605	387.95		
335													0.93601	12.777	0.93601	340.1		
350													1.0211	13.341	1.0211	325.71	0.88496	11.563
400													1.0083	11.528	1.0083	376.96	0.98707	11.285
400																	0.96154	10.993
430													1.0934	11.629	1.0934	373.69		
450													1.1913	12.106	1.1913	358.95	1.119	11.371
500													1.2764	11.674	1.2764	372.24	1.2509	11.44
550																	1.3189	10.966
559																	1.4295	11.695
559																	1.3827	11.312
2	1.1012	15.79													1.1012	6.1		
5	2.9482	16.909													2.9482	5.7268		
10	5.2321	15.004													5.2321	6.45		
15	7.7381	14.794													7.7381	6.55		
20	10.714	15.363													10.714	6.3		
30	14.881	14.225													14.881	6.81		
50	22.619	12.973													22.619	8.2113		
75	31.75	12.14													31.75	7.9767		
90	37.268	11.875													37.268	8.1546		
100	42.182	12.097													42.182	8.0052		
116	50.951	12.596													50.951	7.6879		
128	55.336	12.398													55.336	7.811		
154	64.528	12.016													64.528	8.0589		
179	72.269	11.578													72.269	8.3638		
200	84.969	12.183													84.969	7.9483		
250																		
7																		
10																		
15			0.19399	14.35											0.19399	104.69		
20			0.29704	16.48											0.29704	91.162		
30			0.39403	14.574											0.39403	103.08		
40			0.56983	15.807											0.56983	95.041		
50			0.70926	15.74											0.70926	95.447		
50																		
100			1.2003	13.318											1.2003	112.8		
100																		
150			1.7701	13.094											1.7701	114.73		
150																		
200			2.346	13.015											2.346	115.42		
200																		
250			2.9219	12.968											2.9219	115.84		
250																		
300			3.4069	12.601											3.4069	119.22		
300																		
350			3.9706	12.588											3.9706	119.35		
350																		
400			4.5768	12.696											4.5768	118.33		
400																		
450			4.9466	12.197											4.9466	123.17		
500			5.7105	12.672											5.7105	118.55		
557			6.4379	12.825											6.4379	117.14		
557																		

Nomenclature;   W = width mm;   NDW = non-dimensional width;   Min = mineral oil;   Eth = ethanol

Gap with is rounded off to two decimal places

Table C1. Tabulated data for dimensional and non-dimensional inner-widths.

Flow rate (ml/hr)	W 0.17mm	NDW 0.17mm	W 0.42	NDW 0.42	W 0.90 min	NDW 0.90 min	W 0.60 eth	NDW 0.60 eth	W 0.90	NDW 0.90	W 0.90 WA	NDW 0.90 WA	W 0.60	NDW 0.60	W/delta	Re	W 0.60 WA	NDW 0.60 WA
60											0.051333	17.475			0.051333	857.64		
70											0.058666	16.447			0.058666	911.25		
85											0.058666	13.98			0.058666	1072.1		
100																		
105																		
125									0.080666	15.378	0.058666	11.184			0.058666	1340.1		
150											0.080666	12.815			0.080666	1169.5		
160									0.088	13.107								
175									0.095333	12.982								
185									0.10267	13.225								
200									0.11	13.107	0.10267	12.233			0.10267	1225.2		
225									0.132	13.98								
250									0.13933	13.281	0.12467	11.883			0.12467	1261.2		
275									0.14667	12.709								
300									0.16133	12.815	0.132	10.485			0.132	1429.4		
350									0.20533	13.98	0.16133	10.985			0.16133	1364.4		
400									0.22	13.107	0.18333	10.922			0.18333	1372.2		
450									0.25667	13.592	0.20533	10.874			0.20533	1378.4		
500									0.286	13.631	0.23467	11.184			0.23467	1340.1		
556																		
558.6									0.308	13.139	0.264	11.262			0.264	1330.8		
0																		
7					1.2572	52.803									0.22	1.2572		
8					1.4368	46.203									0.22	1.4368		
10					1.4967	44.355									0.264	1.4967		
15					2.0205	32.855									0.29333	2.0205		
25					2.8063	23.656									0.352	2.8063		
50					5.3172	12.485									0.55733	5.3172		
75					5.0831	13.06									0.77732	5.0831		
100					5.3172	12.485									1.1147	5.3172		
150					5.2312	12.69									1.5106	5.2312		
200					5.5206	12.025									1.7893	5.5206		
250					5.3524	12.403									2.2146	5.3524		
300					5.5794	11.898									2.4786	5.5794		
350					5.4981	12.074									2.8746	5.4981		
400					5.5106	12.047									3.2266	5.5106		
450					5.5893	11.877									3.5346	5.5893		
500					5.6666	11.715									3.9013	5.6666		
559.5																		
0																		
55							0.27699	18.808							0.27699	153.99		
60							0.31023	19.31							0.31023	149.99		
65							0.33239	19.098							0.33239	151.66		
75							0.33239	16.551							0.33239	174.99		
111							0.50967	17.148							0.50967	168.91		
150							0.53183	13.241							0.53183	218.74		
200							0.75342	14.069							0.75342	205.87		
250							0.84206	12.579							0.84206	230.25		
350							1.108	11.822							1.108	244.99		
400							1.3296	12.413							1.3296	233.32		
450							1.5512	12.873							1.5512	224.99		
500							1.7506	13.076							1.7506	221.51		
558.6							1.8392	12.296							1.8392	235.54		

Nomenclature;   W = width mm;   NDW = non-dimensional width;   Min = mineral oil;   Eth = ethanol

Gap with is rounded off to two decimal places